

Article

Phase Diagram Mapping out the Complex Magnetic Structure of Single Crystals of (Gd, Er)B₄ Solid Solutions

Sueli H. Masunaga ^{1,2,*} , Vagner B. Barbeta ¹ , Fábio Abud ^{2,3}, Milton S. Torikachvili ⁴  and Renato F. Jardim ²

¹ Departamento de Física, Centro Universitário FEI, São Bernardo do Campo 09850-901, SP, Brazil; vbarbeta@fei.edu.br

² Instituto de Física, Universidade de São Paulo, São Paulo 05315-970, SP, Brazil; fabio.abud@usp.br (F.A.); rjardim@if.usp.br (R.F.J.)

³ Departamento de Engenharia de Materiais, Escola de Engenharia de Lorena, Universidade de São Paulo, Lorena 12612-550, SP, Brazil

⁴ Department of Physics, San Diego State University, San Diego, CA 92182, USA; miltont@sdsu.edu

* Correspondence: sueli.masunaga@gmail.com

Abstract: Measurements of specific heat and magnetization in single crystals were used to map out the magnetic phase diagram of Gd_{1-x}Er_xB₄ ($x = 0.2$ and 0.4) solid solutions along the c -axis. While GdB₄ orders antiferromagnetically (AF) at 41.7 K, with the easy plane of magnetization oriented perpendicularly to the c -axis, ErB₄ displays AF ordering below 15.4 K, with the easy axis along c . Therefore, in solid solutions, the competition between the different spin anisotropies, as well as frustration, lead to a complex spin configuration. These measurements reveal that a 40% substitution of Er for Gd is sufficient for generating a phase diagram similar to the one for the ErB₄ system, characterized by the occurrence of plateau phases and other exotic features attributed to the interplay of competing magnetic anisotropies.

Keywords: geometric frustration; competing anisotropies; magnetic phase diagram; specific heat; magnetization measurements



Citation: Masunaga, S.H.; Barbeta, V.B.; Abud, F.; Torikachvili, M.S.; Jardim, R.F. Phase Diagram Mapping out the Complex Magnetic Structure of Single Crystals of (Gd, Er)B₄ Solid Solutions. *Magnetism* **2024**, *4*, 24–34. <https://doi.org/10.3390/magnetism4010002>

Academic Editor: Pablo Guardia

Received: 30 November 2023

Revised: 18 January 2024

Accepted: 25 January 2024

Published: 4 February 2024



Copyright: © 2024 by the authors. Licensee MDPI, Basel, Switzerland. This article is an open access article distributed under the terms and conditions of the Creative Commons Attribution (CC BY) license (<https://creativecommons.org/licenses/by/4.0/>).

1. Introduction

The simultaneous occurrence of geometric frustration, competing interactions, and external magnetic fields can result in the appearance of a rich variety of magnetic states with different spin configurations [1–3]. A very well-known geometrical frustrated system is the Shastry–Sutherland lattice, which can be realized in a group of layered compounds [3]. The Shastry–Sutherland model has also been realized in systems displaying magnetization plateaus in the presence of a magnetic field [3–5].

Rare-earth tetraborides with the general composition RB₄ ($R = \text{La-Lu, Pm and Eu}$ excepted) are isostructural, and their crystal structures are tetragonal (space group $P4/mbm$) [6–8]. Most RB₄ have an AF ground state [9], and they may be considered as an experimental realization of the Shastry–Sutherland frustrated system model [10,11]. The geometrical frustration in them is due to the presence of two antiferromagnetic exchange interactions: J_1 between the nearest neighboring (NN) R atoms and J_2 between the next-nearest neighbor (NNN) [11,12]. Although many frustrated compounds are insulating, rare-earth tetraborides are known to be good metals, and their magnetic behavior is determined by Ruderman–Kittel–Kasuya–Yosida (RKKY) interactions [13].

The AF ordering temperature (T_N) in the RB₄ series ranges from $T_N \sim 7$ K for $R = \text{Ho}$ to 44 K for $R = \text{Tb}$ [8]. Some compounds have extra transitions; e.g., $R = \text{Nd, Sm, Tb, Dy, Ho, and Tm}$, and in some cases, these extra transitions are associated with quadrupolar orbital fluctuation [14,15]. ErB₄ undergoes an AF transition at $T_N \sim 15.4$ K, and it has a strong Ising-like anisotropy with the easy axis along the [001] direction. GdB₄ displays an AF transition at $T_N \sim 42$ K, the easy axis is located on the ab -plane, and the system is of Heisenberg-type.

Therefore, the magnetic structure in $\text{Gd}_{1-x}\text{Er}_x\text{B}_4$ mixed compounds should be informed by the competing anisotropies. For magnetic fields parallel or perpendicular to the [001] direction of ErB_4 below T_N , the $M \times H$ curves exhibit a plateau for $M = M_S/2$, where M_S is the saturation magnetization [11,16]. On the other hand, the $M \times H$ curves for GdB_4 below T_N do not show plateaus, perhaps due to the small magnetic anisotropy when compared to the other compounds of the RB_4 family [17].

The origin of the magnetization plateaus is still not fully understood, though they are thought to result from the interplay between anisotropy, Zeeman energy, and frustration, just as other complex magnetic behaviors. For example, in the case of TmB_4 , the applied magnetic field induces an ordered phase with stripes reminiscent of domain boundaries [18]. The origin of the “plateau phase” in ErB_4 is attributed to the competition between the Zeeman energy and the strong anisotropy [11]. Therefore, the change in the delicate balance of these energies can lead to the appearance of new phases, making the magnetic phase diagram of these compounds rich and complex. Given the sensitivity of the overall magnetic behavior to the competing interactions, a study of $\text{Gd}_{1-x}\text{Er}_x\text{B}_4$ solid solutions is in order, since it could help to identify the energetics involved in the various magnetic interactions.

In the case of the $\text{Gd}_{1-x}\text{Er}_x\text{B}_4$ compounds, in addition to the competing anisotropies, which can induce non-conventional spin alignments, the presence of frustration adds a new complication which can result in a complex phase diagram. Systems with competing anisotropies are a matter of intense research [19–21]. It has been shown that solid solutions of isostructural materials with orthogonal anisotropies, subjected to a small concentration of one species, can have spins aligned parallel or perpendicular to the magnetic field, depending on the dominant ion and orientation of the magnetic field. On the other hand, in the intermediate range of concentrations, a new mixed phase with spins pointing neither parallel nor perpendicular to the original easy axis can be induced [22].

The goal of this study was to map out the magnetic phases of $\text{Gd}_{1-x}\text{Er}_x\text{B}_4$ single crystals resulting from the convolution of magnetic frustration and competing anisotropies. High-quality single crystals of $\text{Gd}_{1-x}\text{Er}_x\text{B}_4$ were grown using the flux method and characterized for single-phase composition, crystal quality, and orientation through Laue X-ray and X-ray powder diffraction methods. These single-crystal samples were studied by means of measurements of DC magnetization (M) and specific heat (C_p) as a function of temperature (T) and magnetic field (H). These experiments were performed using a commercial Physical Property Measurement System (PPMS) from Quantum Design. The phase boundary lines were identified in the $H \times T$ phase diagram, and different spin configurations are proposed.

2. Materials and Methods

Single crystals of $\text{Gd}_{1-x}\text{Er}_x\text{B}_4$ ($x = 0.2$ and 0.4) were grown in molten aluminum flux using the methodology described in Ref. [23]. The resulting crystals were shaped like rectangular platelets with in-plane (ab -plane) dimensions in the 1–2 mm range and thicknesses in the 0.5–1.0 mm range. X-ray powder (XRD) analyses and X-ray Laue scans indicated the single-phase nature and high crystallinity of these samples. The characterization of $\text{Gd}_{1-x}\text{Er}_x\text{B}_4$ single crystals has been presented elsewhere [24,25] and is also summarized in the Supplementary Materials.

Specific heat [$C_p(T, H)$] and magnetization [$M(T, H)$] measurements, as a function of temperature, applied magnetic field, and orientation, were performed using the dedicated options of the Physical Property Measurement System (PPMS) from Quantum Design, equipped with a 9 T magnet. The calorimeter relies on a relaxation technique. The samples sat on a sapphire stage that had a minute temperature sensor and a heater underneath. A heat pulse was applied, the temperature of the whole assembly as a function of time was monitored, and the heat capacity was extracted from the relaxation rate [26]. The magnetization was measured using a vibrating sample magnetometer (VSM).

$C_p(T, H)$ data were measured as a function of temperature, ranging from 2 K to 100 K, with magnetic fields up to 9 T applied parallel and perpendicular to the c -axis. The $M(T)$ curves were taken under zero-field-cooling (ZFC) and field-cooling (FC) conditions, with magnetic fields ranging from ~ 5 mT to 9 T, applied parallel and perpendicular to the c -axis. For the ZFC measurements, a sample was first cooled down to 2 K in zero magnetic field; the magnetic field was subsequently applied, and the $M \times T$ data were recorded upon warming up to ~ 300 K. The FC data were collected upon cooling to 2 K following the ZFC cycle. $M(H)$ curves were taken at several temperatures ranging from 4 to 30 K and magnetic fields between -9 and $+9$ T after cooling the crystals in zero applied magnetic field.

3. Experimental Results

Figure 1 shows the specific heat $C_p(T, H)$ for the $\text{Gd}_{1-x}\text{Er}_x\text{B}_4$ ($x = 0.2$ and 0.4) compositions. For $H = 0$ and under the partial substitution of Er^{3+} for Gd^{3+} , the Néel temperature (T_N) decreases from 41.7 K (GdB_4) to ~ 32 K ($x = 0.2$) and to ~ 27 K ($x = 0.4$). For magnetic fields up to 9.0 T, applied perpendicular to the c -axis, T_N shifts slightly to lower temperatures for the $x = 0.2$ and 0.4 compositions, while the overall behavior of $C_p(T, H)$ remains the same, as shown in the lower panels of Figure 1a,b. However, a second shallow maximum centered near 12 K (T_m) develops below T_N in the C_p data for $H \parallel c$, in the 2.9–4.5 T field range for $x = 0.2$, and in the 4.4–6.0 T range $x = 0.4$, as shown in Figures 1a and 1b, respectively. Small bumps in the C_p data also developed near T_m for the $H \parallel ab$ -plane. In the pristine GdB_4 compound, this characteristic was attributed to the Schottky anomaly [27], which is independent of the applied magnetic field [28], and to a hidden transition below which an unusually large magnetoresistance is observed [28]. In the case of $\text{Gd}_{1-x}\text{Er}_x\text{B}_4$, this feature exhibits a slight dependence on the magnetic field for both compositions; as this feature is more responsive to the magnetic field in the $x = 0.4$ samples, it is possible that it arises from competing anisotropies.

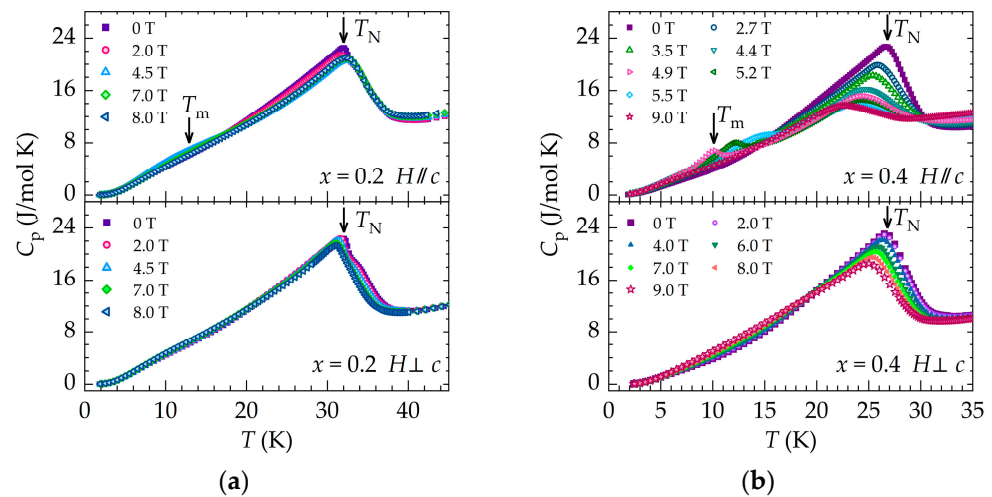


Figure 1. $C_p \times T$ curves under different applied magnetic fields H for $\text{Gd}_{1-x}\text{Er}_x\text{B}_4$ single crystals. (a) $x = 0.2$; (b) $x = 0.4$. Besides the peak at T_N associated with the AF transition, a shallow maximum is also observed at lower temperatures ($T_m \sim 12$ K) along the c -axis.

Isothermal magnetization curves M vs. H below T_N for $H \parallel c$ for the $x = 0.2$ and $x = 0.4$ samples are shown in Figure 2 and Figure S1 in the Supplementary Materials. Unlike ErB_4 , for which the $M(H)$ curves exhibit a magnetization plateau near $M_S/2$ at temperatures as low as 1.5 K [11], this plateau could not be identified in the $\text{Gd}_{0.8}\text{Er}_{0.2}\text{B}_4$ at temperatures as low as 2 K (Figure S1a); only a spin realignment field-induced paramagnetic (FIP) transition could be identified near $H_{\text{FIP}} \sim 4$ T, where the Gd^{3+} moments flip away from the ab -plane. The derivative dM/dH (Figure 2) can be used to monitor the FIP transition and to confirm that a plateau phase is not present. The magnetic phase in fields exceeding H_{FIP} probably corresponds to a fully saturated moment $J = 15/2$ for Er^{3+} . Increasing

temperatures softened the FIP transitions, meaning that the corresponding features in the dM/dH curves could no longer be observed for $T \geq 30$ K.

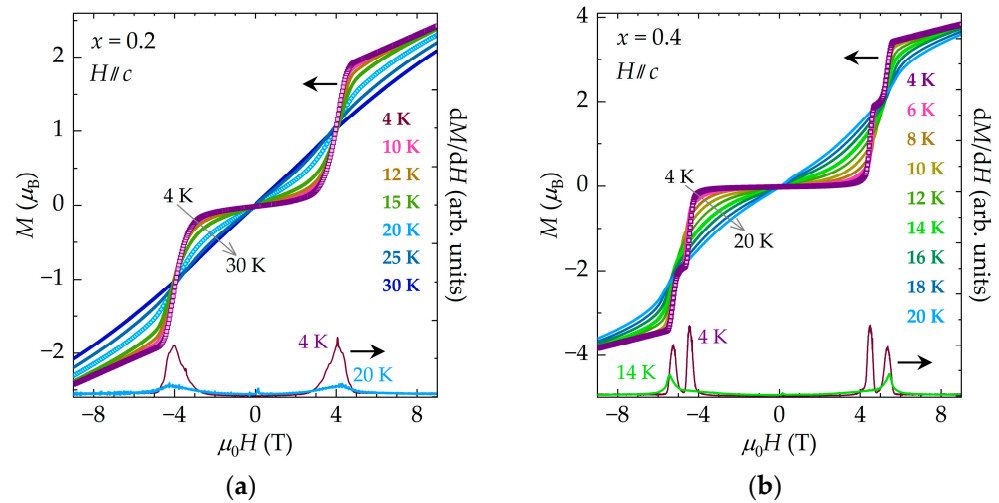


Figure 2. $M \times H$ curves for single crystals of $\text{Gd}_{1-x}\text{Er}_x\text{B}_4$ with (a) $x = 0.2$ and temperatures $T = 4, 10, 12, 15, 20, 25,$ and 30 K and (b) $x = 0.4$ at $T = 4, 6, 8, 10, 12, 14, 16, 18,$ and 20 K. In both cases, the magnetic field H was applied along the c direction. The derivatives dM/dH for two compositions, ranging from -9 T to 9 T, are shown at the bottom of the plots.

On the other hand, the emergence of the plateau phase (PP) can be clearly seen in the $x = 0.4$ samples for $H \parallel c$ between ~ 4.4 and ~ 5.5 T and $T = 4$ K, as shown in Figure S1b. Two features in dM/dH are consistent with the onset and outset of the PP phase, respectively. The transition at ~ 5.5 T is nearly independent of temperature, and the corresponding feature in dM/dH can be identified up to ~ 12 K. Higher temperatures result in a less robust PP transition, meaning that above ≈ 14 K, only the FIP transition can be identified. The maxima in the dM/dH curves characterizing the FIP transitions are clearly identifiable in the isotherms for $T \leq 24$ K. The minor features observed in the dM/dH curves, close to $H = 0$ in both samples, are attributed to changes in slope arising from the presence of remanent magnetization and the coercive field within the magnetic hysteresis loops (Figure S2).

Along the c -axis, the magnetization above H_{FIP} increases linearly with the magnetic field for the $x = 0.4$ samples, and no indication of saturation could be found up to 9 T, the highest field of this experiment. Considering that the Er^{3+} saturation moment (μ_S) is $9 \mu_B$ and that only 40% of the total magnetization is due to the Er^{3+} , it is expected that Er^{3+} contributes $\approx 3.6 \mu_B$ to the total magnetization. Therefore, the jump observed in magnetization as it transitions to the PP region corresponds to approximately half of the Er^{3+} ions changing orientation and aligning with the external magnetic field.

The magnetization curves obtained for $H \perp c$ [25] exhibited just a monotonic increase in magnetization with the applied field for the both $x = 0.2$ and 0.4 samples (Figure S1). This behavior is consistent with the specific heat measurements shown in Figure 1 (lower panels a and b), for which no field-induced phase transition was observed. The reorientation of the spins in GdB_4 [17] and the onset of metamagnetic transitions in ErB_4 [11] take place under applied magnetic fields perpendicular to the c -axis, typically exceeding 12 T. Given that the highest field in our experiment was 9 T, if a similar behavior took place in the $\text{Gd}_{1-x}\text{Er}_x\text{B}_4$ compounds, we would not have been able to observe it.

The behavior of $M/H \times T$ for the $\text{Gd}_{0.8}\text{Er}_{0.2}\text{B}_4$ and $\text{Gd}_{0.6}\text{Er}_{0.4}\text{B}_4$ single crystals obtained under FC conditions is shown in Figure 3. For low field with $H \parallel ab$ -plane and $H \parallel c$, we observed the development of a weak ferromagnetic (wFM) phase, which persisted up to 200 mT. This weak ferromagnetism is quite anisotropic, a behavior reminiscent of RB_4 ($R = \text{Sm}, \text{Gd}$ and Er) when diluted with a nonmagnetic ion [15,24]. The $M/H \times T$ data

collected under FC and ZFC conditions show significant irreversibility up to ~ 100 mT (Figure S3).

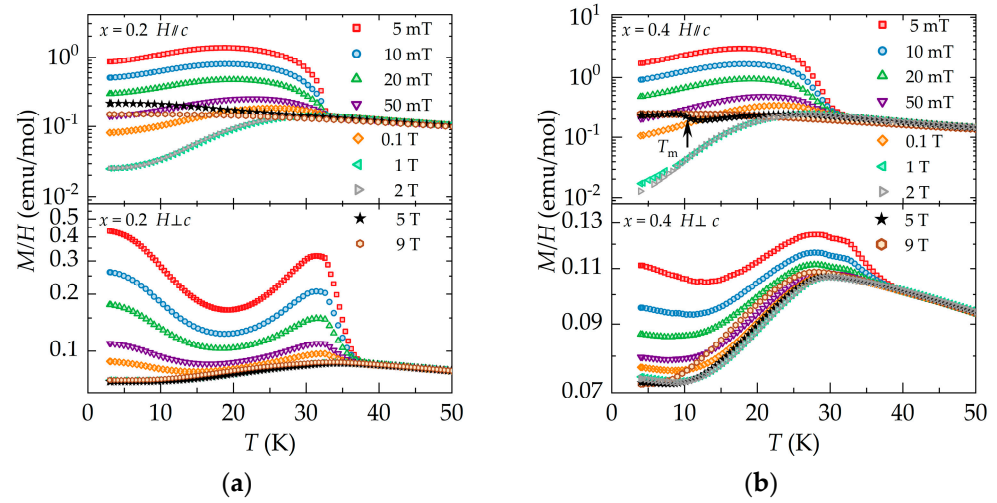


Figure 3. $M/H \times T$ for $\text{Gd}_{1-x}\text{Er}_x\text{B}_4$ samples with (a) $x = 0.2$ and (b) $x = 0.4$ for magnetic fields up to 9 T. The vertical scales are logarithmic to emphasize the field dependence of M/H .

The deconvolution of the components of the wFM can be accomplished by considering that to a first approximation, the magnetization at low fields can be described as follows [24]:

$$M(T) = \chi_0(T)H + M_R(T), \quad (1)$$

where $\chi_0(T)$ is the magnetic susceptibility of the AF sublattice, and $M_R(T)$ is the remnant magnetization corresponding to the wFM phase. $\chi_0(T)$ was selected from the curves obtained within the 2–3 T range, assuming a negligible contribution from the other phases. The $M/H \times T$ curves collapse across the entire temperature range, suggesting the presence of a stable magnetic state. The $M_R(T)$ curves we obtained are shown in Figure 4.

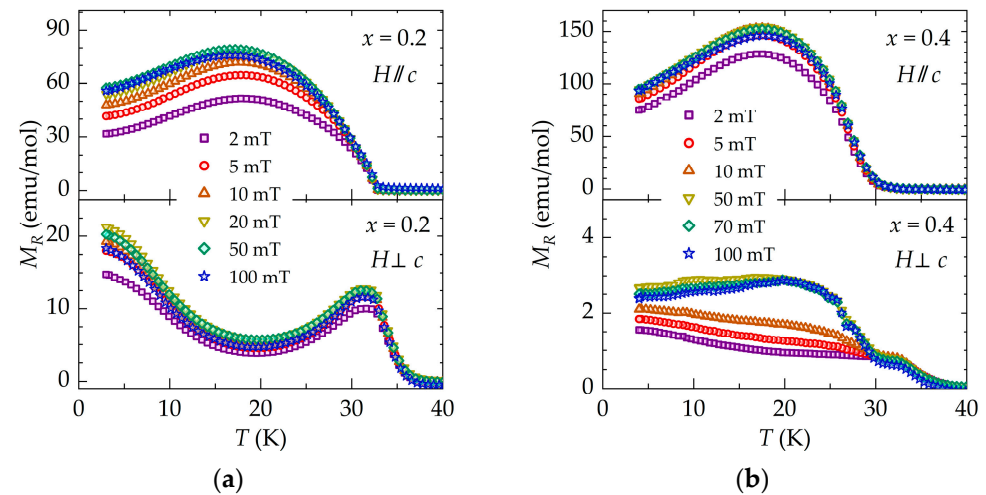


Figure 4. $M_R \times T$ for single crystals of $\text{Gd}_{1-x}\text{Er}_x\text{B}_4$ with (a) $x = 0.2$ and (b) $x = 0.4$ under different external magnetic fields H . The upper panels show the results when the magnetic field H is parallel to the c -axis, and the lower panels show the results for when the magnetic field H was perpendicular to the c -axis.

The $M_R(T)$ data for both samples (Figure 4) show much higher values along the c -axis, which corresponds to the easy axis in ErB_4 . The maximum M_R values along the c -axis amount to 0.19% and 0.35% of the saturated moments (μ_S) for the $x = 0.2$ and 0.4 samples, respectively. In contrast, for the $H \parallel ab$ -plane, these values were reduced to 0.05% and 0.007% of μ_S for the $x = 0.2$ and 0.4 samples, respectively. These values are consistent with the findings for the wFM induced by Y substitution in RB_4 compounds [15]. In the case of RB_4 ($R = \text{Sm, Gd, Tb, Dy, and Er}$) compounds, the highest values of M_R were found for $\approx 30\%$ of Y partial substitution in $\text{R}_x\text{Y}_x\text{B}_4$ [15]. For Gd^{3+} and Er^{3+} , the M_R values correspond to 0.42% and 0.21% of the saturated moments, respectively.

The onset of the wFM for $H \parallel c$ is defined by the inflexion points taking place at ~ 32 K and ~ 27 K for $x = 0.2$ and 0.4, respectively, both below T_N , as shown in the upper panels of Figure 4. This phase emerges at the slightly higher temperatures of ~ 39 K ($x = 0.2$) and ~ 40 K ($x = 0.4$) for the $H \parallel ab$ -plane, values just slightly below $T_N \sim 42$ K for GdB_4 . The data for $H \parallel ab$ -plane suggest that the transitions to the wFM phase take place in two steps, as shown in the bottom panels of Figure 4.

The $M \times H$ data for $H \parallel c$ in the $\text{Gd}_{1-x}\text{Er}_x\text{B}_4$ ($x = 0.2$ and 0.4) compounds reveal remanence and coercivity, as shown in the insets of Figure S1. The magnetic hysteresis for $\text{Gd}_{0.8}\text{Er}_{0.2}\text{B}_4$ persists up to 32 K and 35 K for the $H \parallel c$ and $H \parallel ab$ -plane, respectively. For $\text{Gd}_{0.6}\text{Er}_{0.4}\text{B}_4$, the magnetic hysteresis can be observed up to 30 K for $H \parallel c$; however, M_R and H_C are negligibly small for the $H \parallel ab$ -plane.

The $\text{Gd}_{0.8}\text{Er}_{0.2}\text{B}_4$ sample for the field range from 0.5 to 3.0 T ($H \parallel c$) as well as $\text{Gd}_{0.6}\text{Er}_{0.4}\text{B}_4$ in the 0.5–4.3 T field range both exhibit $M/H \times T$ curves reminiscent of AF systems, displaying a peak near T_N . Examples of such AF-like curves are shown in the upper panels of Figures 3 and S4 for both samples. Conversely, when a magnetic field higher than 0.5 T was applied perpendicular to the c -axis, these characteristics of AF systems were observed in both samples, as shown in the lower panels of Figures 3 and S4.

The metamagnetic transitions observed in the $M \times H$ curves (Figure 2) can also be identified in the $M/H \times T$ curves for $H \parallel c$ (upper panels of Figures 3 and S4) within the 3.5–4.5 T range ($x = 0.20$) and 4.3–6.0 T range ($x = 0.4$). An increase in magnetization with decreasing temperature can be observed below T_N , with the inflection point being identified as the transition temperature. For the $x = 0.2$ samples, this increase cannot be clearly seen given the logarithmic scale of the graph; however, it is indicated in Figure S4a. In the case of the $x = 0.4$ samples, the inflection points at T_m , as depicted in the upper panels of Figures 3b and S4b, correspond to the second peak observed in the $C_p \times T$ curves, as shown in the upper panel of Figure 1b.

Upon further increasing $H \parallel c$, the $M/H \times T$ curves exhibit near saturation at low T , suggesting the complete polarization of Er^{3+} moments for $\mu_0 H \gtrsim 5$ T and 6 T for $x = 0.2$ and 0.4, respectively, as depicted in the upper panels of Figure 3 and Figure S4. This finding is consistent with the trend observed in the $M \times H$ curves shown in Figure 2, where dM/dH displays a peak just below 5 T and 6 T for $x = 0.2$ and 0.4, respectively.

For $H \parallel c$ exceeding 5 T ($x = 0.2$) and 6 T ($x = 0.4$), the magnetization $M(H)$ exhibits linear increases at rates of 0.120 and 0.121 μ_B/T , respectively. Remarkably, these values correspond closely to the 0.121 μ_B/T slope for the GdB_4 measured in Ref. [17]. If this linear trend is maintained, saturation is expected to occur at approximately 50 T and 42 T for $x = 0.2$ and 0.4, respectively. These values are slightly below the saturation field of 54 T observed in the GdB_4 compound, suggesting that the presence of Er^{3+} in the GdB_4 lattice affects the saturation field. It is conceivable that the aligned Er spins might provide an offset field, therefore reducing the applied field necessary to fully saturate the Gd sublattice.

Considering the results described above, the effects of the partial substitution of Er for Gd in $\text{Gd}_{1-x}\text{Er}_x\text{B}_4$ solid solutions can be summarized as follows: (i) an increase in the magnitude of magnetization, as shown in Figure S4, and in the experimentally determined μ_{eff} in the PM state (see, for instance, Reference [25]); (ii) a slight decrease in T_N for the stabilization of the AF state; (iii) an appreciable anisotropy of the wFM phase along the c -axis; and (iv) the stabilization of the plateau state at $\frac{1}{2} M_S$ for the $x = 0.4$ crystals. However,

the transition to the FIP state, certainly related to the presence of Er^{3+} ions, occurs at lower applied magnetic fields ($H_{\text{FIP}} \sim 4$ T) for crystals with $x = 0.2$, whereas it is $H_{\text{FIP}} \sim 5.5$ T for $x = 0.4$, following the emergence of the plateau state at 4.4 T.

We also emphasize that increasing Er concentration in $\text{Gd}_{1-x}\text{Er}_x\text{B}_4$ solid solutions is accompanied by a systematic decrease in the lattice parameters due to the smaller ionic radius of Er [25]. As far as this point is concerned, we might recall that the frustration in the Shastry–Sutherland lattice model is closely related to the competition between the Zeeman effect and interactions J_1 and J_2 . An ordered antiferromagnetic ground state has been found for $J_1/J_2 < 1.43$ [11]. In our solid solutions, due to the partial substitution of smaller Er ions, such a J_1/J_2 ratio is altered and maybe a source of the appearance of the $\frac{1}{2} M_S$ plateau in the $M \times H$ curves.

We also point out that the pristine ErB_4 compound exhibits a strong Ising-type single-ion anisotropy with an easy magnetization axis along the c -axis [4]. On the other hand, the single-ion anisotropy of Gd is considered small, and GdB_4 can be described as a noncollinear Heisenberg antiferromagnet with the easy axis along the (110) direction [29]. Therefore, the partial substitution of Er by Gd has an impact on the magnetic anisotropy of the $\text{Gd}_{1-x}\text{Er}_x\text{B}_4$ solid solution. Such a little but important variation in ionic radii, along with the difference in the magnetic moments between Gd and Er, may, in turn, influence the geometrically frustrated exchange interaction and the exchange couplings, with these effects playing fundamental roles in stabilizing distinct magnetic states [4]. This point is currently under investigation.

4. Discussion

Informed by the detailed magnetization data on the $\text{Gd}_{0.8}\text{Er}_{0.2}\text{B}_4$ and $\text{Gd}_{0.6}\text{Er}_{0.4}\text{B}_4$ single crystals, we were able to assemble field-temperature ($H \times T$) phase diagrams for $H \parallel c$, as shown in Figure 5. The value of T_N decreases slightly for magnetic field $H \parallel ab$ -plane. Given that 9 T is the highest field of this set of data, the phase diagram misses the possible field-induced phase transition at higher fields. Consequently, the $H \times T$ phase diagram for both samples in the ab -plane only includes vertical boundaries delineating paramagnetic (PM), wFM, and AF regions.

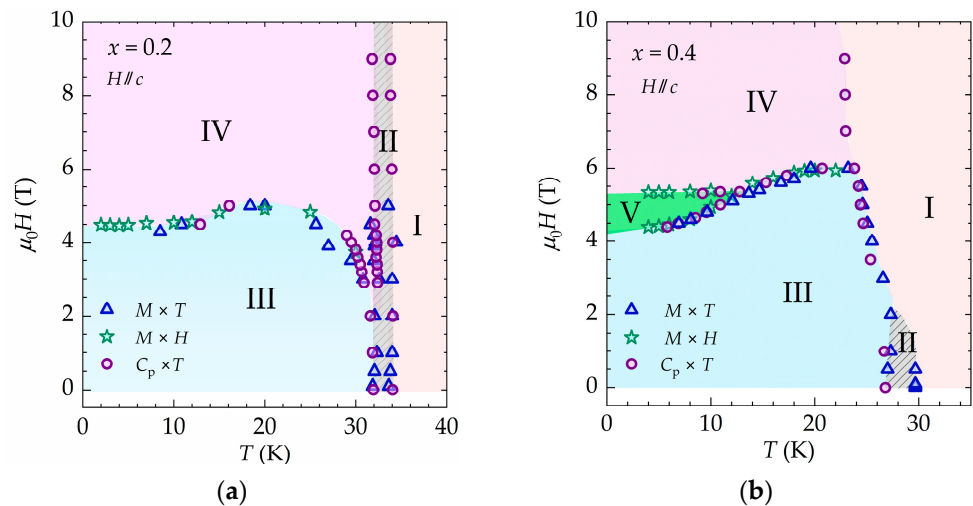


Figure 5. Magnetic phase diagrams for (a) $\text{Gd}_{0.8}\text{Er}_{0.2}\text{B}_4$ and (b) $\text{Gd}_{0.6}\text{Er}_{0.4}\text{B}_4$ for $H \parallel c$. The characteristics of the different phases are discussed in the text. Regions I, II, III, IV, and V correspond to PM, wFM, AF, (FIP + AF), and PP, respectively.

Regions I and II of the phase diagrams in Figure 5 correspond to the paramagnetic PM and wFM phases for $\text{Gd}_{0.8}\text{Er}_{0.2}\text{B}_4$ and $\text{Gd}_{0.6}\text{Er}_{0.4}\text{B}_4$. However, region II for $x = 0.2$ and 0.4 are clearly different. For the $x = 0.2$ samples, a minor anomaly in the $C_p \times T$ data up to $\mu_0 H = 9$ T is observed just above T_N . This anomaly coincides with the onset of the wFM phase, as indicated by the vertical borderline at ~ 34 K. On the other hand, for the $x = 0.4$ samples, there is no corresponding anomaly in the $C_p(H, T)$ data associated with the wFM onset. Our $C_p(H, T)$ and $M(H, T)$ data lack the resolution required to definitively identify the origin of the observed differences in region II for the two Er compositions.

The AF phase was observed to occur within regions III and IV of the phase diagrams for both $x = 0.2$ and 0.4 compositions. The phase boundary between regions I/II and III/IV are clearly correlated with anomalies in the $C_p \times T$ data in applied magnetic fields up to 9 T. In contrast, the ordering temperature is suppressed with increasing magnetic field, as shown in the $M/H \times T$ data, in which saturation in M was observed at low temperatures. Specifically, T_N could be reliably, unambiguously determined from the $M/H \times T$ curves in magnetic fields up to ~ 4.5 T and ~ 6.0 T for the $x = 0.2$ and 0.4 compositions, respectively. Region III represents the AF phase of the $\text{Gd}_{1-x}\text{Er}_x\text{B}_4$ system, whereas region IV denotes the coexistence of the AF phase, associated with the Gd^{3+} sublattice and the FIP phase of the Er^{3+} ions.

The phase boundary between regions III and IV was well defined by the observation of well-defined magnetization jumps observed in the $M \times H$ isotherms for $H \parallel c$. Measurements of $C_p \times T$ and $M/H \times T$ provide limited insight into this boundary due to the small variations in this boundary with H . Phase V (PP), resulting from the plateau at $\frac{1}{2} M_S$ of the Er^{3+} ions, was clearly observed only for the $x = 0.4$ composition. The transitions between phase III and V, as well as between phase V and IV, are characterized by the magnetization discontinuities observed in the $M \times H$ isotherms. The boundary between phases III and V was also clearly delineated through $C_p \times T$ characterization.

Establishing whether the presence of phase V for the $x = 0.2$ composition results from the possible realignment of some of the Er^{3+} spins is quite difficult. In this sample, it is anticipated that the Er sublattice contributes $1.8 \mu_B$ to the overall magnetization of the system. This magnitude is consistent with the observed jump in the $M \times H$ curves, a feature which is very pronounced at $T = 4$ K. As a result, the system appears to transition directly from the AF phase to the mixed phase IV without an intermediate phase V (PP). The temperature of the triple point, in this case, which delineates the boundary lines of phases II, III, and IV, appears to be near 32 K and 3 T.

The phase diagram highlights the role of the partial Er substitution in the GdB_4 lattice and its impact on the boundary lines within the system. For instance, a partial substitution of only 40% of Er for Gd reveals a striking resemblance between the resulting phase diagram (Figure 5b) and that of the ErB_4 compound [11]. Analogous to ErB_4 , the $x = 0.4$ composition displays the presence of two discernible metamagnetic phase transitions, albeit at higher fields. In the ErB_4 phase diagram, derived from neutron diffraction data, three distinct regions identified as being antiferromagnetic, ferrimagnetic, and ferromagnetic merge to a triple point at 11.7 K and 2.1 T [30]. In the $\text{Gd}_{0.6}\text{Er}_{0.4}\text{B}_4$ composition, this triple point is located at ~ 12.8 K, nearly the same temperature as that of ErB_4 , but at a higher magnetic field of ~ 5.4 T, where the phases in region III, IV, and V coalesce, as shown in Figure 5b. Additionally, another triple point can be defined at ~ 24 K and ~ 6 T, where phases I, II, and IV converge.

Remarkably, a partial substitution of just 20% of Er is sufficient for a metamagnetic transition from AF to FIP, as shown in Figure 5a. However, the FIP phase corresponds solely to the orientation of the Er^{3+} ions, as the magnetization corresponds to only 26% and 44% of the theoretical magnetization of $\mu_S = 7.4$ and $7.8 \mu_B$ expected for the $x = 0.2$ and 0.4 compositions, respectively. The complete saturation of the $\text{Gd}_{1-x}\text{Er}_x\text{B}_4$ compounds can be achieved only at saturation fields close to the values found for GdB_4 (i.e., 50 T and 42 T, respectively). In the case of GdB_4 , this metamagnetic transition occurs only at the very high fields of ~ 52 T and ~ 54 T, applied along the a and c axes, respectively [17]. It is important to

emphasize that both the $\text{Gd}_{0.8}\text{Er}_{0.2}\text{B}_4$ and $\text{Gd}_{0.6}\text{Er}_{0.4}\text{B}_4$ compositions exhibit pronounced anisotropies, while the preferred orientation for ErB_4 is the c -axis.

Our combined analysis of the magnetization and specific heat data suggest that the Er and Gd sublattices keep their original easy directions (i.e., the ab -plane for Gd and the c -axis for Er). The possibility of a small canting angle for both easy directions, which would also explain the appearance of the wFM, cannot be completely ruled out.

5. Conclusions

In summary, we relied on the magnetization and specific heat data for $\text{Gd}_{0.8}\text{Er}_{0.2}\text{B}_4$ and $\text{Gd}_{0.6}\text{Er}_{0.4}\text{B}_4$ to construct a magnetic phase diagram detailing a set of complex magnetic structures. Notably, for both samples, the Néel temperature drops slightly for the $H \parallel ab$ -plane, while the occurrence of a field-induced plateau phase in fields below 9 T ($H \parallel c$) is specific to the $x = 0.4$ compositions. Therefore, the phase diagram focuses primarily on the emergence of phases for $H \parallel c$. We have identified five different regions in the phase diagrams. Regions I to IV for $x = 0.2$ comprise paramagnetic, weak ferromagnetic, antiferromagnetic, and mixed field-induced paramagnetic and antiferromagnetic phases. A plateau phase composed of the $\frac{1}{2} M_S$ plateau state (PP) was found for the $x = 0.4$ compositions.

The phase diagrams displayed in Figure 5 summarize the effect of the partial substitution of Er for Gd in the GdB_4 lattice, and the boundary lines were experimentally determined along the c -axis using the $M \times T$, $M \times H$, and $C_p \times T$ curves. In the $\text{Gd}_{1-x}\text{Er}_x\text{B}_4$ compounds, the exchange couplings J_1 and J_2 , which play an essential role in stabilizing distinct magnetic states, were altered due to the differences between Gd and Er ionic radii, as well as differences in magnetic moment and single-ion anisotropy. Contrary to classical competing anisotropy systems, such as $\text{Fe}_{1-x}\text{Co}_x\text{Cl}_2$ [31], $\text{Fe}_x\text{Ni}_{1-x}\text{F}_2$ [32], and others, it is important to point out that a tiny ($\sim 20\%$) partial Er substitution is sufficient for inducing a metamagnetic transition from the antiferromagnetic state to the field-induced paramagnetic state. Also, we observed that a 40% Er substitution results in a phase diagram closely resembling that of ErB_4 . Both compositions studied exhibit strong anisotropies favoring the c -axis, the easy axis for ErB_4 . These findings provide insights into the interplay of the magnetic phases as a c -axis easy-axis ion partially replaces an ab -plane easy-orientation ion.

Supplementary Materials: The following supporting information can be downloaded at: <https://www.mdpi.com/article/10.3390/magnetism4010002/s1>, magnetism—Supplementary Materials: Figure S1. $M \times H$ curves under $H \parallel c$ and $H \perp c$ for single crystals of $\text{Gd}_{1-x}\text{Er}_x\text{B}_4$ with (a) $x = 0.2$ at $T = 2$ K; (b) $x = 0.4$ at $T = 4$ K. The arrows indicate the sweeping direction of the applied magnetic field. The insets show an expanded view of the low-field limits of the curves; Figure S2. $M \times H$ under $H \parallel c$ for single crystals of $\text{Gd}_{1-x}\text{Er}_x\text{B}_4$ with (a) $x = 0.2$ at $T = 20$ K; (b) $x = 0.4$ at $T = 14$ K. The corresponding derivatives, dM/dH , for both compositions are presented at the bottom of the plots; Figure S3. $M/H \times T$ for $\text{Gd}_{1-x}\text{Er}_x\text{B}_4$ samples with (a) $x = 0.2$ and (b) $x = 0.4$ measured under magnetic fields up to 0.1 T. The closed symbols represent zero-field-cooled (ZFC) curves, while the open symbols depict field-cooled (FC) curves, as indicated by the arrows; Figure S4. $M/H \times T$ for $\text{Gd}_{1-x}\text{Er}_x\text{B}_4$ samples with (a) $x = 0.2$ and (b) $x = 0.4$ measured under magnetic fields ranging from 0.5 T to 9.0 T in the FC process. The shallow maxima observed at T_m in the $C_p(T)$ curves correspond to the inflexion points in the $M/H \times T$ curves (marked by the arrows in the figure).

Author Contributions: Conceptualization, R.F.J.; formal analysis, S.H.M. and V.B.B.; investigation, S.H.M., F.A., R.F.J. and M.S.T.; resources, R.F.J.; writing—original draft preparation, S.H.M. and V.B.B.; writing—review and editing, F.A., R.F.J. and M.S.T.; supervision, R.F.J.; funding acquisition, R.F.J. All authors have read and agreed to the published version of the manuscript.

Funding: This research was funded by FAPESP (Grants No. 2013/07296–2, 2019/26141–6, 2022/02691–0, and 2022/10874–7), CNPq (Grant No. 301463/2019–0), and CAPES (Finance Code 001).

Institutional Review Board Statement: Not applicable.

Informed Consent Statement: Not applicable.

Data Availability Statement: The data presented in this study are available upon request.

Conflicts of Interest: The authors declare no conflicts of interest.

References

1. Seabra, L.; Momoi, T.; Sindzingre, P.; Shannon, N. Phase diagram of the classical Heisenberg antiferromagnet on a triangular lattice in an applied magnetic field. *Phys. Rev. B* **2011**, *84*, 214418. [[CrossRef](#)]
2. Gabani, S.; Flachbart, K.; Siemensmeyer, K.; Mori, T. Magnetism and superconductivity of rare earth borides. *J. Alloys Compd.* **2020**, *821*, 153201. [[CrossRef](#)]
3. Brunt, D.C.; Balakrishnan, G.; Mayoh, D.; Lees, M.R.; Gorbunov, D.; Qureshi, N.; Petrenko, O. Magnetisation process in the rare earth tetraborides, NdB₄ and HoB₄. *Sci. Rep.* **2018**, *8*, 232.
4. Farkašovský, P.; Regeciová, L. Formation of Magnetization Plateaus in Rare Earth Tetraborides: Exact Diagonalization and Quantum Monte Carlo Studies. *J. Supercond. Nov. Magn.* **2020**, *33*, 3463–3467. [[CrossRef](#)]
5. Pristáš, G.; Bačkai, J.; Orendáč, M.; Gabáni, S.; Gažo, E.; Shitsevalova, N.; Dukhnenko, A.; Siemensmeyer, K.; Flachbart, K. Magnetic Phase Diagram of Geometrically Frustrated Magnetic System ErB₄ under High Pressure. In Proceedings of the International Conference on Strongly Correlated Electron Systems (SCES2019), Okayama, Japan, 23–28 September 2019.
6. Fisk, Z.; Maple, M.B.; Johnston, D.C.; Woolf, L.D. Multiple phase transitions in rare earth tetraborides at low temperature. *Solid State Commun.* **1981**, *39*, 1189–1192. [[CrossRef](#)]
7. Etourneau, J.; Mercurio, J.P.; Berrada, A.; Hagenmuller, P.; Georges, R.; Bouezg, R.; Gianduzzo, J.C. The magnetic and electrical properties of some rare earth tetraborides. *J. Common Met.* **1979**, *67*, 531–539. [[CrossRef](#)]
8. Yin, Z.P.; Pickett, W.E. Rare-earth–boron bonding and 4f state trends in RB₄ tetraborides. *Phys. Rev. B* **2008**, *77*, 035135. [[CrossRef](#)]
9. Buschow, K.H.J. Magnetic Properties of Borides. In *Boron and Refractory Borides*; Matkovich, V.I., Ed.; Springer: Berlin/Heidelberg, Germany, 1977; pp. 494–515. ISBN 978-3-642-66620-9.
10. Watanuki, R.; Sato, G.; Suzuki, K.; Ishihara, M.; Yanagisawa, T.; Nemoto, Y.; Goto, T. Geometrical Quadrupolar Frustration in DyB₄. *J. Phys. Soc. Jpn.* **2005**, *74*, 2169–2172. [[CrossRef](#)]
11. Michimura, S.; Shigekawa, A.; Iga, F.; Sera, M.; Takabatake, T.; Ohoyama, K.; Okabe, Y. Magnetic frustrations in the Shastry–Sutherland system ErB₄. *Phys. B Condens. Matter* **2006**, *378–380*, 596–597. [[CrossRef](#)]
12. Inami, T.; Ohwada, K.; Matsuda, H.Y.; Wen, O.Z.; Nojiri, H.; Matsumura, T.; Okuyama, D.; Murakami, Y. Resonant Magnetic X-ray Diffraction Study on Successive Metamagnetic Transitions in TbB₄. *J. Phys. Soc. Jpn.* **2009**, *78*, 033707. [[CrossRef](#)]
13. Schäfer, W.; Will, G.; Buschow, K.H.J. The magnetic structure of the rare earth tetraborides ErB₄ and DyB₄. *J. Chem. Phys.* **1976**, *64*, 1994–1997. [[CrossRef](#)]
14. Okuyama, D.; Matsumura, T.; Nakao, H.; Murakami, Y. Quadrupolar Frustration in Shastry–Sutherland Lattice of DyB₄ Studied by Resonant X-ray Scattering. *J. Phys. Soc. Jpn.* **2005**, *74*, 2434–2437. [[CrossRef](#)]
15. Kang, B.Y.; Lee, S.S.; Song, M.S.; Cho, K.K.; Han, S.H.; Cho, B.K. Universality of weak ferromagnetism in the magnetically frustrated system R_{1-x}Y_xB₄. *Curr. Appl. Phys.* **2016**, *16*, 1001–1004. [[CrossRef](#)]
16. Mat’áš, S.; Siemensmeyer, K.; Wheeler, E.; Wulf, E.; Beyer, R.; Hermannsdörfer, T.; Ignatchik, O.; Uhlarz, M.; Flachbart, K.; Gabáni, S.; et al. Magnetism of rare earth tetraborides. *J. Phys. Conf. Ser.* **2010**, *200*, 032041. [[CrossRef](#)]
17. Kikkawa, A.; Katsumata, K.; Narumi, Y.; Suga, K.; Fukui, T.; Sugaya, T.; Kindo, K.; Iga, F.; Michimura, S. Magnetization Process in GdB₄. *J. Phys. Soc. Jpn.* **2007**, *76*, 024711. [[CrossRef](#)]
18. Siemensmeyer, K.; Wulf, E.; Mikeska, H.-J.; Flachbart, K.; Gabáni, S.; Mat’áš, S.; Priputen, P.; Efdokimova, A.; Shitsevalova, N. Fractional Magnetization Plateaus and Magnetic Order in the Shastry–Sutherland Magnet TmB₄. *Phys. Rev. Lett.* **2008**, *101*, 177201. [[CrossRef](#)]
19. Katsumata, K.; Tawaraya, T. Tetracritical behaviours of random mixtures with competing spin anisotropies. *J. Magn. Magn. Mater.* **1980**, *15–18*, 253–254. [[CrossRef](#)]
20. Mano, H. Pair-Spin Theory of a Random Mixture with Competing Ising and XY Anisotropies. *J. Phys. Soc. Jpn.* **1986**, *55*, 908–919. [[CrossRef](#)]
21. Katsumata, K.; Shapiro, S.M.; Matsuda, M.; Shirane, G.; Tuchendler, J. Simultaneous ordering of orthogonal spin components in a random magnet with competing anisotropies. *Phys. Rev. B* **1992**, *46*, 14906–14908. [[CrossRef](#)]
22. Mano, H. Possible Phase Diagrams of Systems with Competing Anisotropies. *Prog. Theor. Phys. Suppl.* **1990**, *101*, 597–610. [[CrossRef](#)]
23. Fisk, Z.; Cooper, A.S.; Schmidt, P.H.; Castellano, R.N. Preparation and lattice parameters of the rare earth tetraborides. *Mater. Res. Bull.* **1972**, *7*, 285–288. [[CrossRef](#)]
24. Masunaga, S.H.; Barbeta, V.B.; Jardim, R.F.; Becerra, C.C.; Torikachvili, M.S.; Rosa, P.F.S.; Fisk, Z. Anomalous remnant magnetization in dilute antiferromagnetic Gd_{1-x}Y_xB₄. *Phys. Rev. Mater.* **2018**, *2*, 084415. [[CrossRef](#)]
25. Masunaga, S.H.; Barbeta, V.B.; Abud, F.; Torikachvili, M.S.; Jardim, R.F. Anomalous Ferromagnetic Phase in the Gd_{1-x}Er_xB₄ Series: Crystal Growth, Thermal, and Magnetic Properties. *Crystals* **2023**, *13*, 1137. [[CrossRef](#)]
26. Hwang, J.S.; Lin, K.J.; Tien, C. Measurement of heat capacity by fitting the whole temperature response of a heat-pulse calorimeter. *Rev. Sci. Instrum.* **1997**, *68*, 94–101. [[CrossRef](#)]
27. Novikov, V.V.; Mitroshenkov, N.V.; Morozov, A.V.; Matovnikov, A.V.; Avdashchenko, D.V. Heat capacity and thermal expansion of gadolinium tetraboride at low temperatures. *J. Appl. Phys.* **2012**, *111*, 063907. [[CrossRef](#)]

28. Cho, B.K.; Rhyee, J.-S.; Kim, J.Y.; Emilia, M.; Canfield, P.C. Anomalous magnetoresistance at low temperatures ($T \leq 10\text{K}$) in a single crystal of GdB_4 . *J. Appl. Phys.* **2005**, *97*, A923. [[CrossRef](#)]
29. Johnston, D.C. Magnetic Susceptibility of Collinear and Noncollinear Heisenberg Antiferromagnets. *Phys. Rev. Lett.* **2012**, *109*, 077201. [[CrossRef](#)] [[PubMed](#)]
30. Pfeiffer, F.; Schäfer, W.; Will, G.; Etourneau, J.; Georges, R. The magnetic phase diagram of ErB_4 . *J. Magn. Magn. Mater.* **1979**, *14*, 306–308. [[CrossRef](#)]
31. Wong, P. Specific-Heat Study of Random-Field and Competing-Anisotropy Effects in $\text{Fe}_{1-x}\text{Co}_x\text{Cl}_2$. *Phys. Rev. B* **1986**, *34*, 1864–1879. [[CrossRef](#)]
32. Perez, F.A.; Borisov, P.; Johnson, T.A.; Stanescu, T.D.; Trappen, R.; Holcomb, M.B.; Lederman, D.; Fitzsimmons, M.R.; Aczel, A.A.; Hong, T. Phase Diagram of a Three-Dimensional Antiferromagnet with Random Magnetic Anisotropy. *Phys. Rev. Lett.* **2015**, *114*, 097201. [[CrossRef](#)] [[PubMed](#)]

Disclaimer/Publisher’s Note: The statements, opinions and data contained in all publications are solely those of the individual author(s) and contributor(s) and not of MDPI and/or the editor(s). MDPI and/or the editor(s) disclaim responsibility for any injury to people or property resulting from any ideas, methods, instructions or products referred to in the content.